

connected everything.

industrial systems in the digital age

Design & Manufacture of Novel 3D Printed Electrodes

Dr Daniel Niblett (PI)

Dr Hosni Elwan (RA)

Dr Keerthana Jaganathan (RA)

Newcastle University



EPSRC

Engineering and Physical Sciences
Research Council

Summary

Feasibility Projects:

1. Prototype Implicit Diffusion Model for Fast Image Characterisation

- Daniel Niblett

2. Genetic Algorithm for Image Optimisation

- Daniel Niblett

3. Neural Network for Effective Diffusivity Modelling

- Keerthana Jaganathan

4. 3D printing of electrodes using digital light printing and fuel cell integration

- Hosni Elwan, Daniel Niblett

Abstract

Electrochemical devices offer a possible route towards decarbonisation and electrification of energy conversion and storage. Electrolysers, fuel cells and redox flow batteries all use common electrode or electrode supporting materials; some of which are porous and stochastic. In this study we evaluate the feasibility of designing, optimising, manufacturing and testing porous materials from the ground up, moving from stochastic to structured materials.

Physics models (Implicit diffusion model) is created to predict the effective diffusivity on a 3D voxel grid representing a porous structure. This is then used to generate 5000 images of random porous structures to train a neural network model as a surrogate for the physics-based model. A voxel based genetic algorithm is developed to optimise the porous structure to maximise effective diffusivity under porosity constraints. Structured cubic lattice digital materials are 3D printed with UV digital light printing methods, carbonised and tested in hydrogen polymer electrolyte fuel cell.

Feasibility Study Questions

There were 3 components to the feasibility study which highlights the connected nature of the work. The goal of the study was to develop a framework that can optimise a porous structure (given an objective and under constraints) then manufacture that structure using tools today. Initial questions of the study were as follows:

1. Is it possible to design a framework to optimise the microstructure of porous electrodes without human input?
2. Can machine learning be used to assist in the computation cost of computational fluid dynamics simulations?
3. What are the limitations of current digital and additive manufacturing tools?
4. How do the structured materials perform in real electrochemical cells?

Project Team



PI

Dr Daniel
Niblett



RA

Mr Hosni Elwan



RA

Dr
Keerthana
Jaganathan

Project 1 - 4

- Modelling
- Genetic Algorithm
- 3D printing

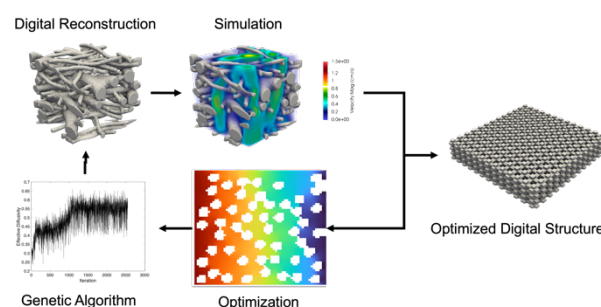
Project 4

- 3D printing
- Carbonisation
- Fuel cell testing

Project 3

- Neural network model

Industrial Partner: Photocentric – Paul Holt and Rob Young have provided critical 3D printing expertise and consultant meetings regarding the 3D printing, resin and carbonisation work.



Project Output

1. Presented work at the 244th Electrochemical Society Annual Meeting, Gothenburg, Sweden, October 2023¹
2. Code for implicit diffusion on 3D voxel grids for steady state diffusion reaction equation.
3. Prototype of voxel based genetic algorithm for optimisation of porous structure.
4. Neural network model trained on physics-based simulations with high accuracy and low cost.
5. Manufactured structured carbon porous materials with 10 μm fibre and 50 μm pore radius.

¹ Hosni Elwan, Daniel Niblett, Mohamed Mamlouk, Porous Electrode Optimization for PEMFCs Using 3D Printing Technology, 244th ECS Meeting (October 8-12, 2023)

6. Tested and characterised materials as cathode in fuel cells.

$$\Delta C = \frac{J}{D} \left(\frac{2L_1}{A_1} + \frac{L_2}{A_2} \right)$$

Feasibility Project 1: Prototype Implicit Diffusion Model for Fast Image Characterisation

Inside a volume, the presence of solid phases (porous structure) introduces local diffusive flux variations. If a concentration gradient is applied to the boundaries of this volume and the volume is discretised into many small volumes with connecting faces, the Laplace equation can be solved using computational fluid dynamics (CFD) to predict the resulting concentration field.

Motivation

To start it is useful to determine what are the possible improvements by replacing stochastic materials with structured materials (as a benchmark for an optimised material).

Starting with a unit cell for a structured lattice:

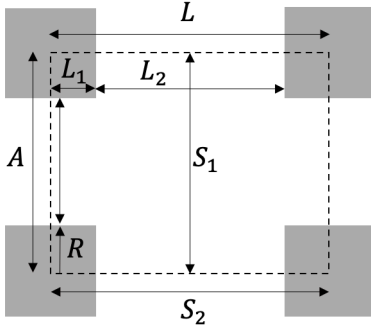


Figure 1 – Unit cell for a cubic lattice in 2D where solid particles are shown in gray.

The resistive nature of this material against fluid or species flow can be predicted both analytically and numerically by considering Fick's Law of diffusion and Hagen-Poiseuille equation.

$$J = \frac{D_e A}{L} \Delta C$$

$$Q = \frac{kA}{\mu L} \Delta P$$

Diffusion

At steady state the molar and mass flows are equal and therefore the pressure difference between the inlet and outlet is equal to the sum of resistor blocks in parallel:

$$\Delta C = \Delta C_1 + \Delta C_2 + \Delta C_3$$

Where the subscripts 1 and 2 represent the pore

throat and pore body faces. In this scenario, $L_1 = R$ and $L_2 = L - 2R$. The cross-sectional areas are taken in three-dimensions as:

$$A_1 = (L - 2R)^2$$

$$A_2 = \left(\frac{L^2 + A_1}{2} \right)$$

Combining all the terms allows the ratio of the effective to the bulk diffusivity to be found:

$$J = \frac{D_e A}{L} \frac{J}{D} \left(\frac{2L_1}{A_1} + \frac{L_2}{A_2} \right)$$

$$\frac{D_e}{D} = \frac{L}{A \left(\frac{2L_1}{A_1} + \frac{L_2}{A_2} \right)}$$

This can then be rearranged to predict the diffusivity as a function of the unit cell length and the radius of the fibres:

$$\frac{D_e}{D} = \frac{1}{2L^2 \left(\frac{R}{(L - 2R)^2} + \frac{(L - 2R)}{L^2 + (L - 2R)^2} \right)}$$

This equation was compared against computational fluid dynamics, by solving the Laplace equation on a structured grid with the results shown in Figure 2.

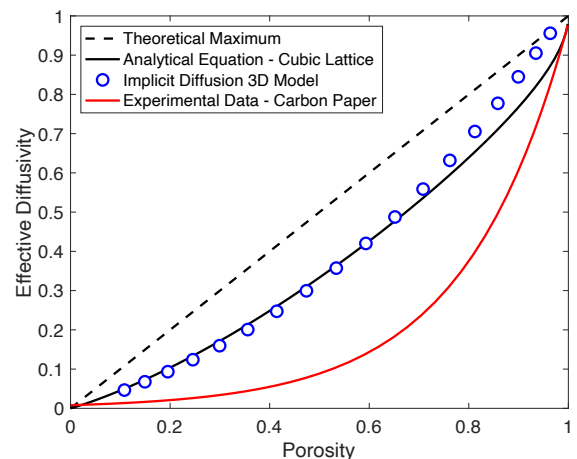


Figure 2 – Effective diffusivity of cubic lattice and carbon paper microstructures as a function of porosity. Blue circles are extracted from the 3D physics-based model, black solid

line is analytical prediction and the red line is a fit from experimental data of carbon paper.

The analytical model results (black line) hold up reasonably well against the CFD results and therefore it can be used reliably to predict the effective diffusivity for cubic unit lattices as shown in Figure 3.

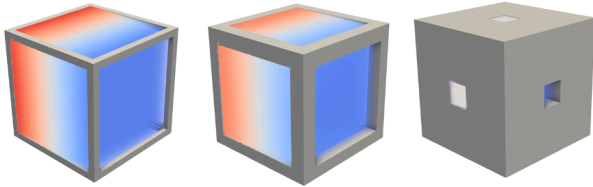


Figure 3 - Unit cubic lattice microstructures, with solved concentration field from CFD shown

The colour field shows the concentration field in the structures. On figure 2, a fit of experimental data results for carbon paper (used as supporting electrode material in fuel cells, electrolyzers and redox flow batteries) is shown in red².

It is clear that the effective diffusivity of the structured materials is far larger than that of carbon paper and therefore it should offer lower resistance for oxygen diffusion to the catalyst layer of fuel cells.

Permeability

At low Reynolds numbers (i.e. viscous force dominating flows) the flow through the cubic lattice pores and pore throats is a linear relationship to the pressure gradient³. Deriving the permeability in a similar way to diffusion an analytical equation for permeability is:

$$K = \frac{L}{A \left(\frac{2R}{\left(\frac{L^2}{4} - LR + R^2 \right) \beta_1 A_1} + \frac{4L - 8R}{L^2 \beta_2 A_2} \right)}$$

where the constants β_1 and β_2 are related to the square cross-sections as:

$$\beta_i = \left[\frac{1}{3} - \frac{64H_i}{\pi^5 W_i} \tanh \left(\frac{\pi W_i}{2H_i} \right) \right]$$

Where H_i and W_i are half the cross-section faces heights and width respectively for each face. Data for cubic lattice permeability exists and is compared against the analytical permeability estimation in Figure 4.

Without any empirical factors, given the fibre radius and unit lattice size, the permeability can be predicted with good accuracy. Furthermore, the permeability of the

cubic lattice structures is larger than that of carbon paper at the same porosity.

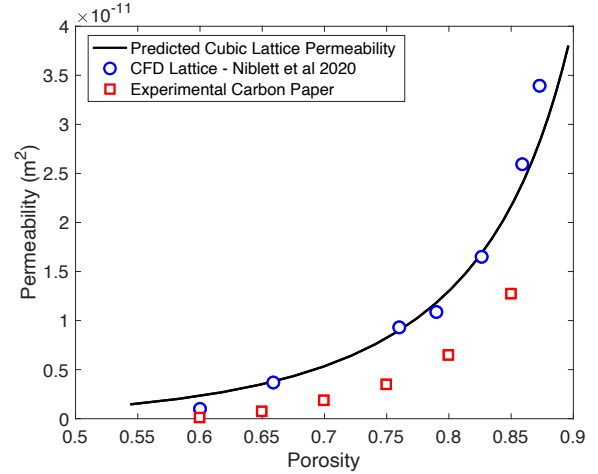


Figure 4 - Cubic lattice permeability as a function of porosity. Black line shows the analytical equation, blue dots are CFD data from literature and red squares are experimental data for carbon paper⁴.

Both analytical predictions show a larger diffusivity and permeability than carbon paper which provides promising motivation for the study.

Microstructure Development

Algorithms from the Porous Microstructure Generator was used to generate random particles in two dimensions (this was done to speed up objective function evaluation for the genetic algorithm.) This generates an image as shown in Figure 5.

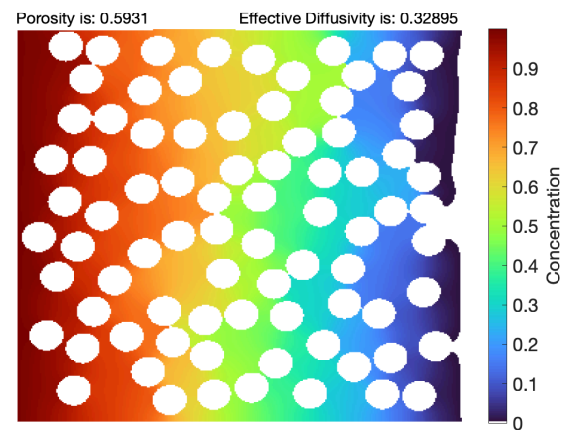


Figure 5 - Image and solved concentration field of a 2D random porous microstructure with the solid circular particles shown in white and a 1 to 0 concentration difference.

A finite volume method model to solve the concentration field in response to a concentration difference applied to the inlet and outlet was

² Ismail, M. S., et al. "Effective diffusivity of polymer electrolyte fuel cell gas diffusion layers: An overview and numerical study." *International Journal of Hydrogen Energy* 40.34 (2015): 10994-11010.

³ Niblett, Daniel, Stuart Martin Holmes, and Vahid Niasar. "Discrete-particle model to optimize operational conditions of proton-exchange membrane fuel-cell gas channels." *ACS*

Applied Energy Materials 4.10 (2021): 10514-10533.

⁴ Niblett, Daniel, Vahid Niasar, and Stuart Holmes. "Enhancing the performance of fuel cell gas diffusion layers using ordered microstructural design." *Journal of The Electrochemical Society* 167.1 (2019): 013520.

developed in MATLAB. At steady state, the sum of all flux j_{ij} into each cell is equal to zero:

$$\sum j_{ij} A_{ij} = 0$$

The flux through each cubic face between volume i and volume j is described by Fick's law of diffusion:

$$j = \frac{D_{ij} A_{ij}}{L_{ij}} (C_i - C_j)$$

where the constants can be combined into a conductivity term:

$$G_{ij} = \frac{D_{ij} A_{ij}}{L_{ij}}$$

In one dimension, the flux into each volume is therefore:

$$-\frac{D_{i1} A_{i1}}{L_{i1}} (C_i - C_{j1}) + \frac{D_{i2} A_{i2}}{L_{i2}} (C_i - C_{j2}) = 0$$

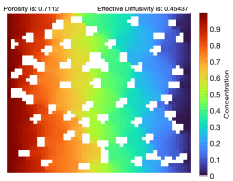
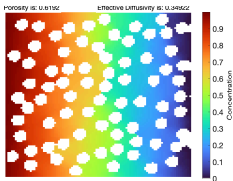
Combining the terms and expanding to three dimensions reveals the equation in the coefficient form:

$$\begin{aligned} -G_{i1} C_i + G_{i2} C_i + G_{i1} C_{j1} - G_{i2} C_{j2} &= 0 \\ (G_{i2} - G_{i1}) C_i &= G_{i1} C_{j1} - G_{i2} C_{j2} \\ a_p C_p &= \sum a_{nb} C_{nb} + S_p \end{aligned}$$

Which can be solved by iterative linear solvers with the coefficients:

$$a_p = \sum a_{nb} + S_p$$

This implicit algorithm is coded into a Matlab script and the conductivity coefficients are set to zero to ensure there is no gradient in concentration at the solid surfaces. At the boundaries, the constant values are coded as an implicit source term on the inlet and outlet patches.

Grid Size	Simulation Speed (s)	Image
50	0.63	
100	1.15	

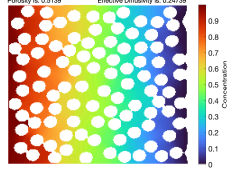
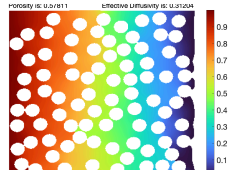
200	5.1	
300	20.95	

Figure 6 – Performance (simulation speed) of the steady state diffusion algorithm at different grid resolutions. Using lower grid size will result in less accurate image.

As Figure 6 shows, increasing grid resolution will increase the computation time. Regardless, this 2D diffusion simulation captures the effect of the porous structures on the concentration field and thus it can be used for fast objective function evaluation.

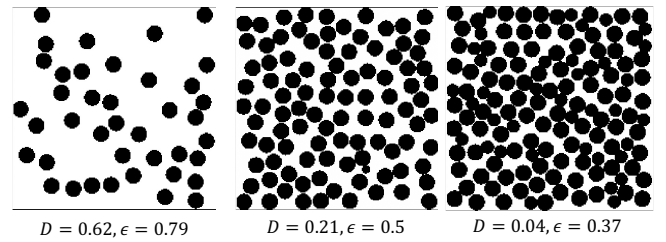


Figure 7 - Examples of images and characterisation provided to neural network and genetic optimisation algorithms.

As shown by Figure 7, a binary image of a microstructure (which can be 2D or 3D) can have information encoded (e.g. diffusivity and porosity). These images were then used to train a neural network to test the feasibility of developing a surrogate model to provide an alternative objective function evaluator in contrast to the finite volume method simulation presented above. Although in this case the simulation is relatively quick, industrially relevant simulations can be in the order of hours to weeks for one simulation and with significant resources.

5000 Microstructures with randomised porosity was generated and simulated with a grid resolution of 200 x 200 cells. This required around 7 hours of serial computation time.

Feasibility Project 2: Genetic Algorithm for Image Optimisation

Motivation

The aim of this project was to develop an evolutionary based genetic algorithm for optimising a porous structure given an objective function (provided by physics-based models) and manufacturing constraints (from 3D printing).

Challenges

1. The algorithm must be decoupled from the simulation method, allowing it to be versatile to handle any structure optimisation problem.
2. It must conserve porosity and not violate minimum feature size requirements (e.g. isolated binary pixels are not resolvable for realistic simulation conditions)

Model Development

The development of the model started by learning how to construct a genetic algorithm from the ground up in MATLAB. The objective function model would be the diffusion model in the previous project and algorithm should maximise diffusivity (D) under a porosity constraint.

$$\begin{aligned} &\max D \\ &\text{subject to } \epsilon = \text{constant} \end{aligned}$$

The evolutionary optimisation algorithm was developed as follows:

1. Create initial population set
2. Simulate diffusion on images
3. Rank order the simulation images based on fitness for probability of selection.
4. For each new offspring structure pair, use roulette wheel selection to choose parent structures.
5. Use cross-over methods to create offspring materials with shared characteristics of the parents.
6. Apply mutation to evolve and advect the surface under porosity and parent feature constraints (using custom PMG features).
7. Re-apply the procedure and track diffusivity, porosity over time.
8. Break the algorithm when a tolerance is met.

Initial Challenges

The traditional genetic algorithm will not work for this type of volumetric based microstructures because the conductive phase must be continuous. This means that

randomised inverting of binary pixels (traditionally performed in binary GA, or a scalar value in continuous GA) will not be sufficient as this can happen inside or near to a solid wall, creating under-resolved regions.

Therefore, new cross-over and mutation algorithms were created for this purpose diffusion-based processes.

There are several hyper-parameters related to the operation of the GA, however it runs independently to the simulation code (thus highlighting its applicability to be coupled to other modelling methods). These parameters are:

- Mutation probability, Mutation magnitude, cross-over probability, Elitism ratio, number of candidates.

Initial Prototype

We know from the analytical models of structured materials in Figure 2 that straight and lattice type microstructures can provide higher diffusivity. And the most optimal arrangement would be a bundle of tubes, aligned normal to the direction of the concentration gradient. We will show how our initial model can approximate this:

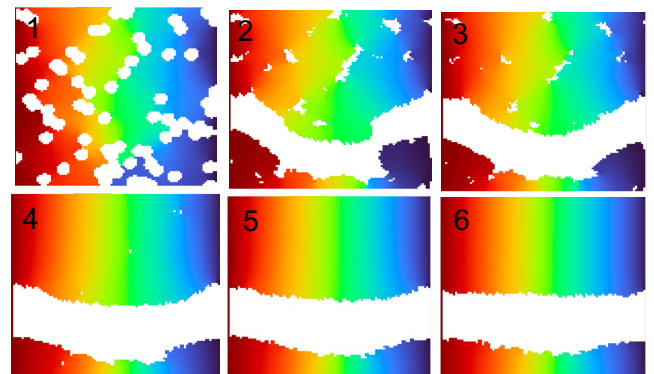


Figure 8 - Microstructure evolution from a randomised set to optimized solution using pixel based genetic algorithm, with solved concentration fields.

Figure 8 shows a clear transition between generations to the optimal shape (being a straight line) but reaching a local minimum due to the concentration of initial particles being closer to the bottom boundary. After point 2, the algorithm becomes more influenced by mutation, since parents will not be so different to each other.

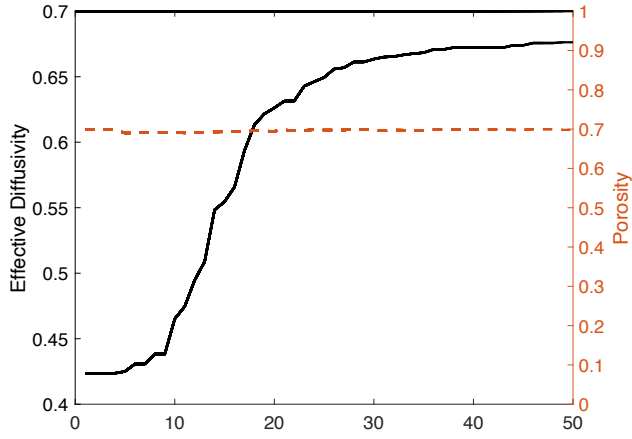


Figure 9 – Shows the change in effective diffusivity for each generation for the microstructures in Figure 8. The dashed line shows the constant porosity.

Figure 9 shows the algorithm working, increasing the effective diffusivity from 0.43 to 0.66 at a constant porosity of 70%. The rate of change of the fitness begins to plateau as it reaches the theoretical maximum. It is possible that larger, dynamic and adaptive mutation could push the algorithm closer the maximum (but at the cost of more generation cycles). In this example our simulation cost is relatively small and so this required only 2 minutes to complete (4 candidates, 30% mutation, 100% crossover, 25% elitism).

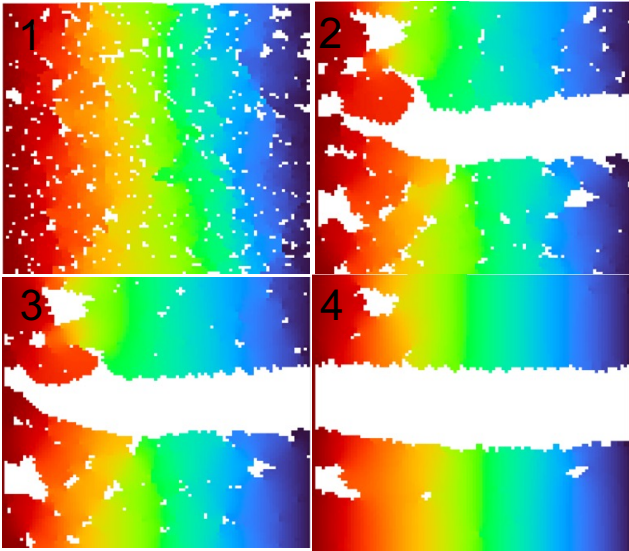


Figure 10 – Example of a different optimization case, starting from random point initialization. The initialization can determine the final structure shape/location.

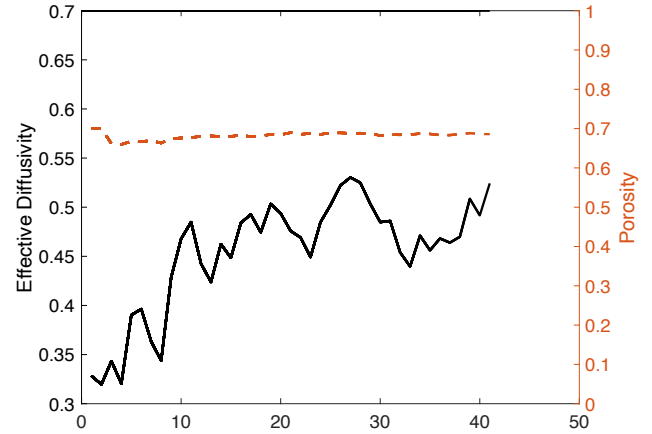
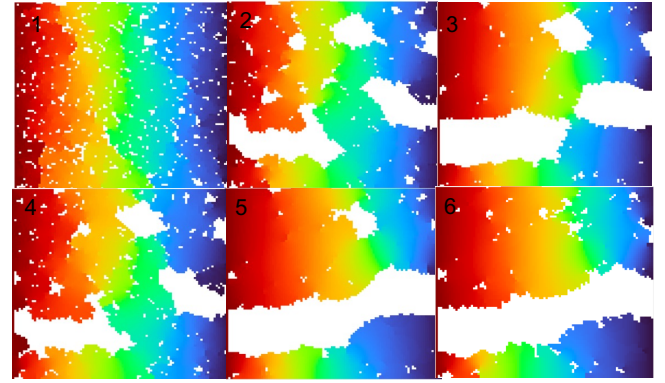


Figure 11 – Multi-objective optimization with the algorithm attempting to maximise both effective diffusivity and interfacial area.

Figure 11 shows the algorithm working under multi-objective optimisation. In this case, maximise diffusivity and surface area, and in practice this is achieved by multiplying the fitness by the inverse of the rank ordered microstructures based on surface area (to reduce its probability for selection).

For multi-objective optimisation, it is most optimal if the fitness value encompasses a variety of parameters lumped into that term (e.g., efficiency for electrolyzers).

To test the GA for other simulation methods, a surface reaction term was coded into the implicit diffusion solver, where the mass flow is conserved:

$$0 = -\sum G_{ij}(C_i - C_j) - N_i k_i C_i$$

This means that there is an implicit source/sink term on the interface cells, dependent on the surface concentration. The coefficient matrix is simply amended as:

$$a_p = \sum G_{nb} + N_i k_i$$

Now the fitness function will be to maximise the surface concentration, or reaction rate (to mimic the need to increase oxygen concentration at the catalyst layer of fuel cells).

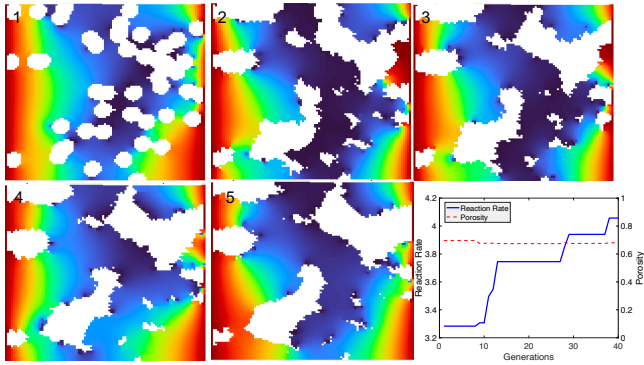


Figure 12 - Maximizing surface reaction rate in a porous structure with concentration sources from both sides of the domain

Figure 12 shows that the change in the structure improves the reaction rate from 3.3 to 4.1 while maintaining a constant porosity. This time it did not form a straight line, which is promising, instead the structure merged together regions of small pore size (which are limiting in diffusion) and instead created larger open pores and increased the surface roughness (and therefore surface area).

The optimisation required 40 generations of 4 candidates each, requiring 120 simulations to reach an optimal solution. This highlights the need to tune the evolutionary algorithm using the fast diffusion model presented above, before coupling it with more complex predictive simulations.

Outputs

1. Pixel based genetic algorithm developed for microstructure optimisation.
2. Optimised materials for effective diffusivity in 2D.
3. Coupled the GA to external CFD simulation.

Future Work

1. Upgrade the cross-over and mutation methods for faster optimisation.
2. Couple algorithm to more complex simulations (e.g. Navier-Stokes equations).
3. Extend the framework to 3D, allowing the structures to be 3D printed.

Feasibility Project 3: Neural Network for Effective Diffusivity Modelling

Motivation

The computational cost and speed of complex computational fluid dynamic simulations can be large. If the output of the simulation is a single metric (e.g. efficiency, resistance etc.) that characterises a geometry or image, then machine learning algorithms may be able to be used as a surrogate model.

Methodology

In our research study, we employed a combination of Convolutional Neural Networks (CNNs) and the Convolutional Block Attention Module (CBAM) in our model.

We chose CNNs because of their ability to automatically identify essential features in images, a crucial requirement for our image-based prediction tasks. To further enhance our model's performance, we integrated CBAM, which focuses on key regions or features within the images. This attention mechanism is mainly helpful for complex images like 2D porous electrodes. CBAM allowed our model to intelligently prioritize specific areas and channels within the feature maps, resulting in more effective feature extraction and ultimately improving the accuracy of our predictions.

Resources

In our study, we employed Keras, Google Colab, Python and GPU runtime to develop and train our CNN-CBAM model for image-based effective diffusivity prediction of 2D porous electrodes.

Deep Learning Framework: **Keras**
Development Environment: **Google Collab** with GPU resources
Programming Language: **Python**

There is relevant literature on predicting transport properties in porous materials using machine learning and deep learning methods ⁵⁶

Neural Network Details

Our Network Architecture is designed to process image-based data representing porous electrode structures efficiently. The architecture consists of the following key components:

Convolutional Layers:

The first convolutional layer consists of 128 neurons, providing the model with the capacity to extract high-level features from the 2D electrode structure images.

The second convolutional layer consists of 64 neurons, balancing feature extraction and computational efficiency.

Max-pooling layer-down samples feature maps, preserving critical structural information.

The outputs from both branches are concatenated to leverage the complementary information captured by different convolutional pathways, ensuring a comprehensive understanding of the porous electrode structure.

Attention Mechanism (CBAM):

CBAM, integrated into the model, adaptively highlights relevant regions and channels within the 2D image data. This feature is instrumental in achieving precise diffusivity predictions.

Global Pooling Layers:

Global average and max pooling layers summarise information from the entire 2D image, reducing dimensionality and enhancing model generalisation.

Dense Layers:

The number of neurons in these layers is carefully tuned through experimentation to optimise the model's capacity to recognise detailed patterns within 2D porous electrode images.

Resources

Datasets for diffusion simulations on 2D porous material images were completed using the algorithm in project 2. In total 5000 images were generated and characterised to train the ML model.

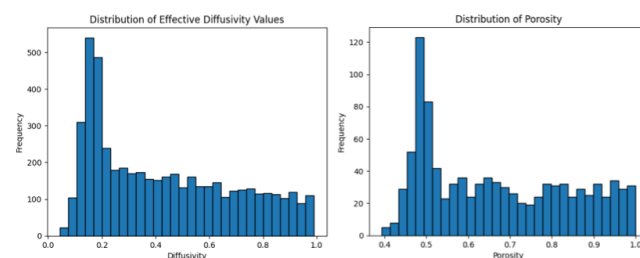


Figure 13 - Diffusivity and porosity distributions of the training datasets

Optimisation Algorithm: The Adam optimisation algorithm was used to update the network's weights

⁵ Graczyk, K. M., Strzelczyk, D., & Matyka, M. (2023). Deep learning for diffusion in porous media. *Scientific Reports*, 13(1). <https://doi.org/10.1038/s41598-023-36466-w>

⁶ Cawte, T., & Bazylak, A. (2023). Accurately predicting transport properties of porous fibrous materials by machine learning methods. *Electrochemical Science Advances*, 3(1).

and biases during training.

Validation: The training dataset was split into training and validation sets to monitor model performance and prevent overfitting.

Best Model selection: The model with the highest coefficient of determination (R-squared) on the validation set is selected as the best model.

Model Evaluation: The best model is loaded and evaluated using the independent test data (unseen data during training). Its performance is assessed by R-squared and mean square error (MSE) metrics.

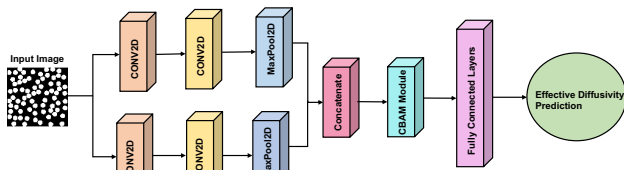
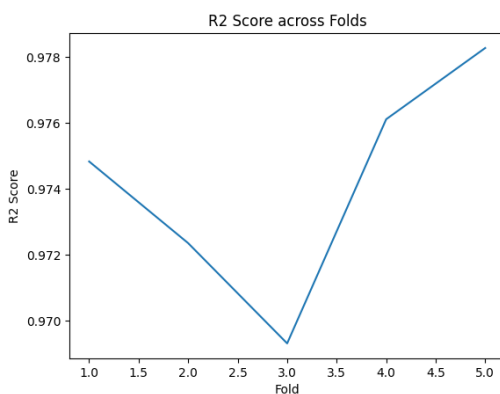


Figure 14 - Schematic of the network architecture for predicting effective diffusivity of images

Training Data Details

Resizing: To standardise images to a uniform size (128x128 pixels) for consistent input to deep learning models, a prerequisite for most machine learning algorithms while simplifying computational processing.

Normalisation: Scaling down pixel values from 0 to 255 to a range between 0 and 1, ensuring consistent feature scales. Normalisation prevents issues like gradient explosions, promotes faster model convergence, and enhances generalisation to new data.



The trained model was able to predict the diffusivity values of the dataset with high accuracy (97%). However, these images are simplified spherical particles and training on other more complex microstructures may be a challenge.

Future Work

The training was performed with a large number of datasets. For future work, it is necessary to reduce the training dataset to a small number (e.g. 2 – 50) which

is reasonable to generate using complex computational fluid dynamic simulations.

A highly accurate model may not be required, as accuracy in the order of 90% for complex simulations and microstructures will be important.

Feasibility Project 4: 3D printing of electrodes using digital light printing and fuel cell integration

Motivation

The optimisation algorithm presented in project 2 has the ability to generate pixel (and therefore voxel when extended to 3D) images. This discrete information about the distribution of solid materials in a 3D space can be manufactured using layer-by-layer additive manufacturing.

Digital Design

This project is about testing the feasibility, and whilst structures presented in Project 1 are not the most optimal for all scenarios, they provide a basis to test the capability of 3D printers for electrode manufacturing.

The digital design of the porous electrodes was created through microstructure reconstruction algorithms, developed for the Porous Microstructure Generator (PMG)⁷. By specifying the pore size and fibre size different cubic lattice, the microstructure can be generated as an image stack (.tiff) and a surface (.stl) as shown by Figure 15.

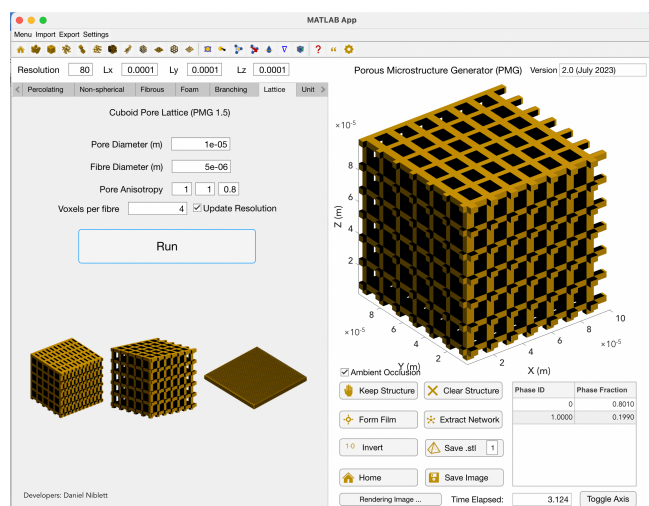


Figure 15 – Example of cubic lattice generated by PMG.

The limitations of LCD UV light 3D printing, restrict feature sizes of 5 times the pixel resolution⁸. The Phrozen Sonic Mini 8k has a XY pixel resolution of 22 μm , and therefore the limitation on feature sizes is around 100 μm , but it could be extended further than this. For this study we used a pore size of 200 μm and fibre size of 100 μm :

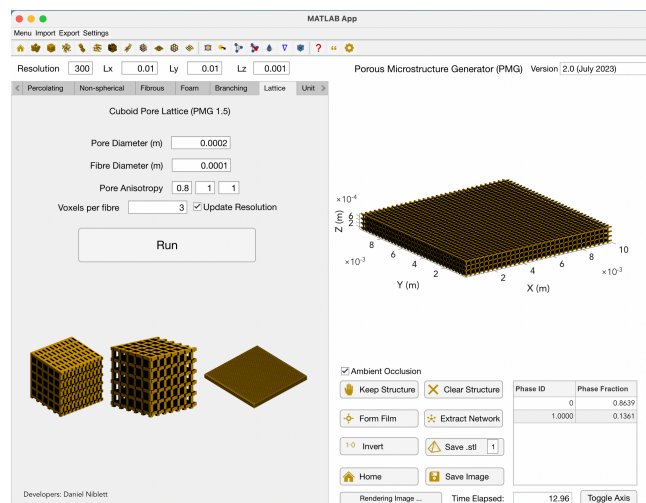


Figure 16 - Example of 10 x 10 x 1 mm electrode sample, with 200 μm pore and 100 μm fibre diameters made with PMG.

For most electrochemical devices, the electrodes are thin but have a large cross-sectional area. Traditional materials such as carbon paper has thicknesses between 100 – 300 μm . Carbonisation will shrink printed polymer feature sizes >50%, meaning the resulting thickness will be around 500 μm . As shown by Figure 16, generation of this structure in PMG only requires 12 seconds, allowing for fast digital prototyping. A variety of other microstructures can be made with PMG including those shown by Figure 17.

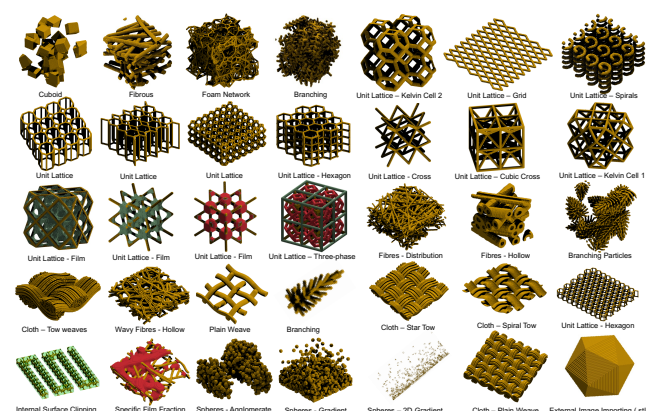


Figure 17 - Abstract of different microstructures able to be produced by PMG

⁷ Niblett, Daniel; Mamlouk, Mohamed; Emmanuel Godinez Brizuela, Omar; An, Senyou (2022). Porous Microstructure Generator, Newcastle University. Software. <https://doi.org/10.25405/data.ncl.20448471.v7>

⁸ Niblett, Daniel, et al. "Utilization of 3D printed carbon gas diffusion layers in polymer electrolyte membrane fuel cells." *International Journal of Hydrogen Energy* 47.55 (2022): 23393-23410.

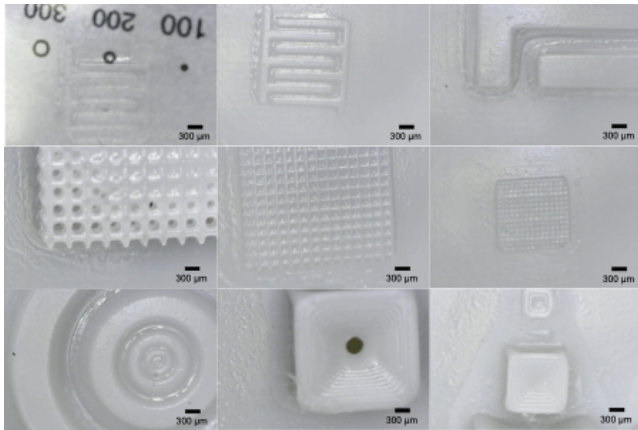


Figure 18 – Initial 3D printing tests to understand feature sizes.

Figure 18 shows the printers ability to print different microstructural shapes, in some instances, the resin gets over-exposed and blocks some of the porous structures. Part of the challenge of printing thin porous structures is getting them to detach from the build plate, and without structure damage.

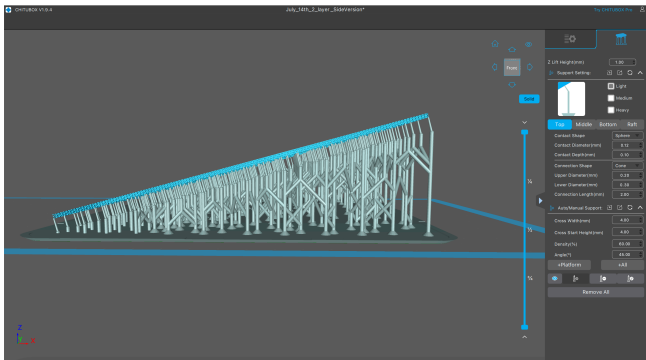


Figure 19 - Visualisation of the slicing software used to slice the geometry and supports (10° angle, 200 µm cone supporting connections and at 2.3 seconds per layer exposure).

The distribution of support structures, often automatically generated by the slicing software can be an issue, as shown by Figure 19. The proximity of some pillars can lead to structural damage during printing.

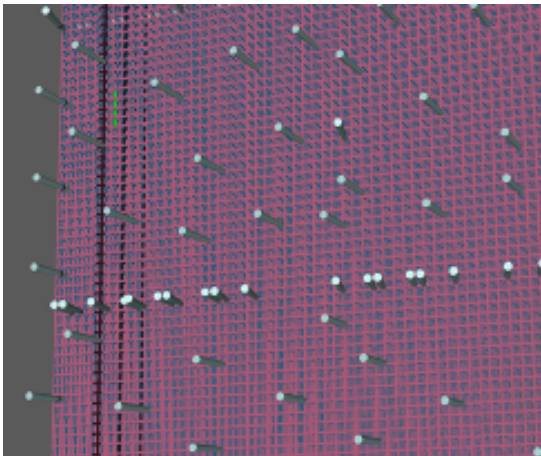


Figure 20 - Distribution of automatic support structures

Initial Results

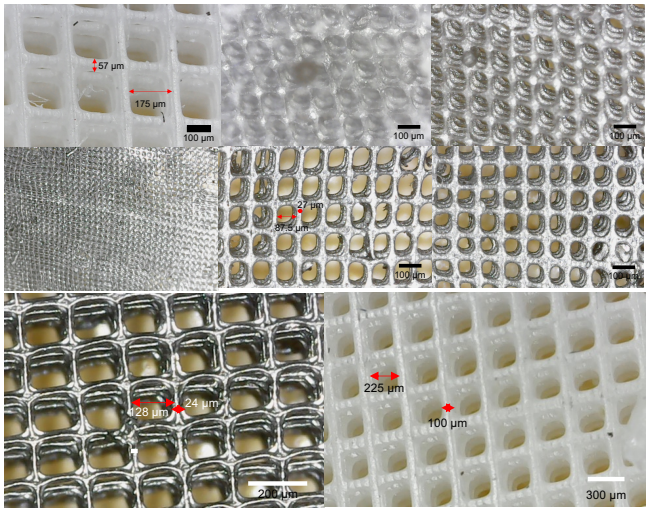


Figure 21 - Optical microscope images of printed and carbonised microstructures

	3D printed	Carbonised	% of original
Pore Size (µm)	225	128	56%
Fibre Size (µm)	100	24	24%

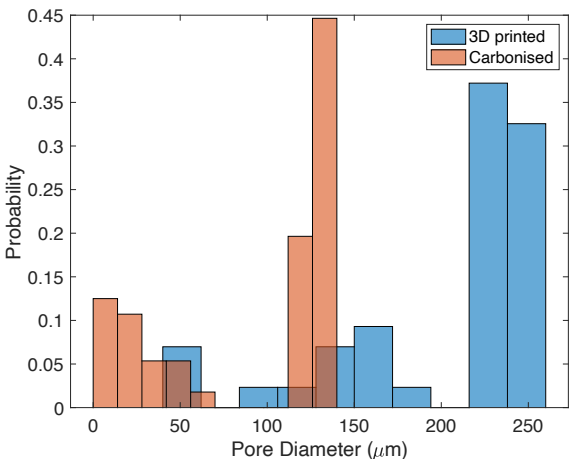


Figure 22 - Shrinkage results of feature sizes after carbonisation using image analysis tools.

The pores are preserved during the printing and carbonisation processes. One challenged faced by the digital design is the digital size of the files. As shown by Figure 23, the size of these files can easily reach GB and this will be more pronounced with smaller feature sizes. Currently the files are between 30 – 600 GB/m2 of thin electrode materials. One solution to this would be to bypass the slicing stage all together and use the image stacks generated by PMG to the printer.

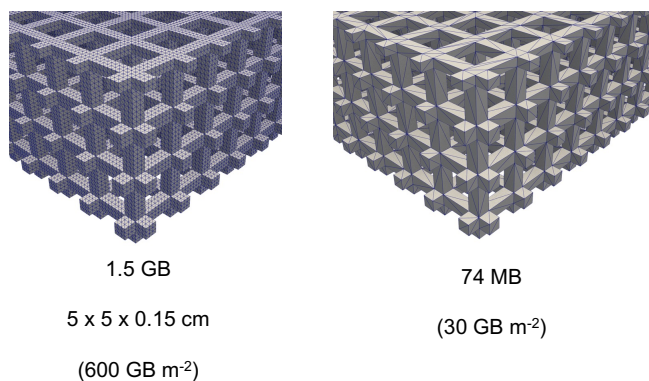


Figure 23 - File sizes and surface triangulation of large scale 3D printed materials

Washing and Curing

A specialized cleaning apparatus, outfitted with a solvent, is utilized to cleanse the freshly printed items. As an illustration, IPA is the chosen solvent for the aqua resin. This procedure is pivotal to remove any residual resin from the surface following the printing process. Once cleaned, the samples are aerated to dispel the solvent. Afterwards, they are transitioned to a curing chamber for a duration of an hour, facilitating the completion of the photopolymerization. To guarantee the samples maintain a flat orientation post-curing, a stabilizing weight is strategically positioned atop them during the curing procedure.

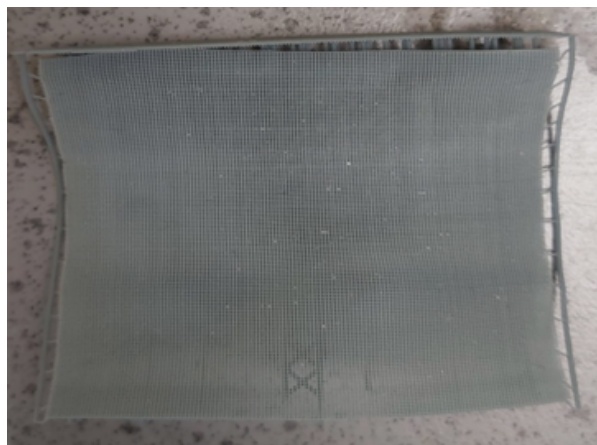


Figure 24 - 3D structure after washing and curing step.

Carbonisation

Once the GDL is printed, a tubular furnace was utilized to carbonize the sample, enhancing its electrical conductivity, making it a suitable GDL for LT-PEMFC. A Thermolyne® 21100 tube furnace (Figure 2) was used to carbonize the 3D GDL samples, which is equipped with Eurotherm temperature controller (3216 CP) that support temperature programming.

The samples undergo carbonization in a tube furnace under a nitrogen (N₂) atmosphere, with temperatures ranging from 30 to 900°C. Before this process, a thermogravimetric analysis (TGA) was performed to determine the temperature at which significant weight

loss occurs.

An isothermal TGA test, designed to replicate the conditions in the tube furnace during carbonization, was then conducted Figure 23. The initial heating to 200°C, at a swift rate of 10°C/min, primarily resulted in the evaporation of residual solvents such as IPA, accounting for a 4 wt.% reduction. Between 200 and 500°C, there was a substantial weight reduction of around 76 wt.% reflecting main decomposition. From 500 to 900°C, a minor 20 wt.% weight reduction was observed, likely due to the reconfiguration of polymeric carbon chains, enhancing electrical conductivity.

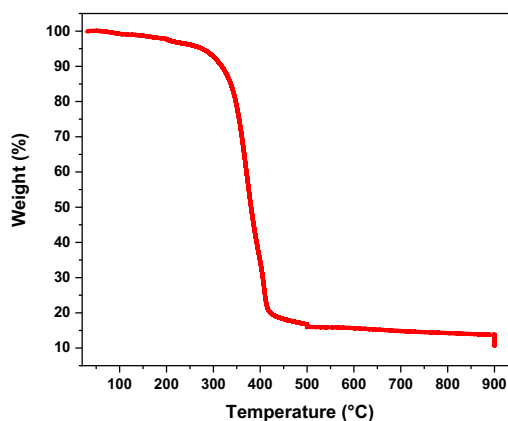


Figure 25 - Isothermal TGA test for the mass loss of printed photopolymer

Considering the results from both the rapid and isothermal TGA tests, the temperature parameters for carbonization were established in Figure 26. The carbonization process took a total of 600 minutes.

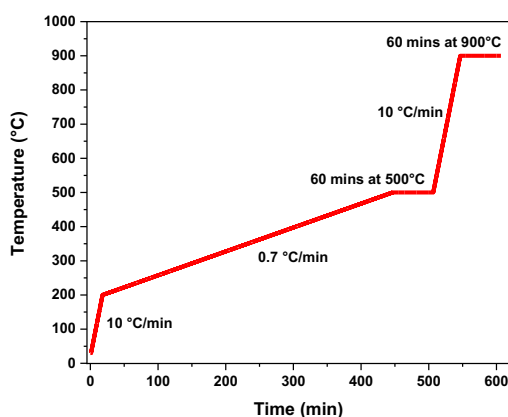


Figure 26 - Temperature settings used to carbonize the 3D samples.

Carbonisation Challenges

During the carbonization process, the sample undergoes thermal decomposition, causing it to curl. This could result in an uneven surface, which is not ideal for fuel cell applications. To address this, we wrapped the sample in a Ni weave prior to carbonization, ensuring it remained flat throughout the process as shown by Figure 27. Post-carbonization,

the sample was observed to have shrunk by 50%.

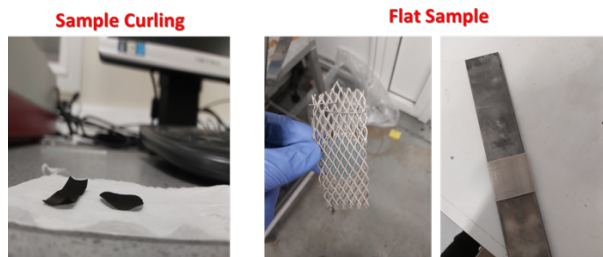


Figure 27 – Examples of sample curling and methods used to flatten samples during carbonisation

It's important to note that the resin's composition influences the sample's thermal decomposition behaviour. For instance, when we utilized the Phrozen Water-Washable 3D Printing Resin, the samples were notably sensitive to temperature fluctuations within the tube furnace. This sensitivity led to significant damage to the sample (Figure 28), even when the temperature settings remained consistent. However, when this resin was substituted with the aqua resin, the latter proved more resilient to temperature variations, making the carbonization process more consistent and reliable.



Figure 28 - Damaged carbonized sample based on the water washable resin

Electrical Conductivity

After carbonization, the electrical conductivity of the sample was measured using The EverBeing R-2 Four-Point Probe device. For the 3D sample, a current of 0.3 A is applied, and the subsequent voltage drop is observed over 30 seconds using the chronopotentiometry method. This procedure is conducted five times on various parts of the sample, and the average value is then determined. The in-plane electrical resistance recorded was 0.15Ω , a value substantially lower (by a factor of nearly four) than the commercial GDL Freudenberg H23C9, which has a resistance of 0.7Ω . The in-plane electrical conductivity was calculated to be 18913.13 S/m . This indicates that the carbonization process effectively enhanced the electrical conductivity of the 3D sample.

SEM and X-ray Tomography

To analyse the printed structure morphology, both scanning electron microscopy and X-ray computed tomography was used (in collaboration with Dr. Adrian Mularczyk from Eindhoven).

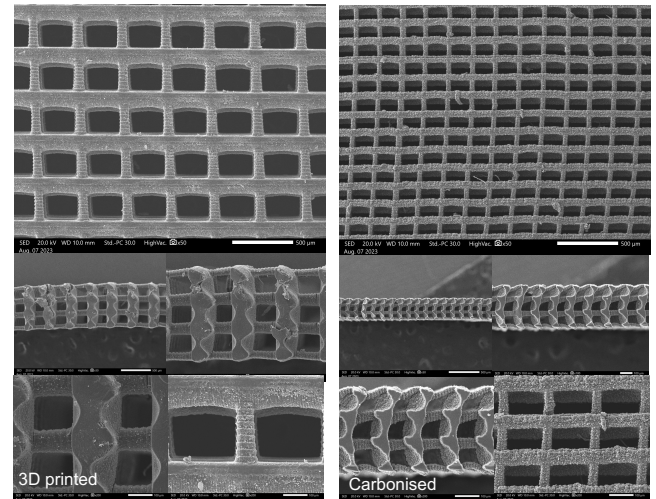


Figure 29 - SEM image of 3D printed and carbonised materials at the same scale in each image set. The carbonised samples exhibited shrinkage of >50%.

The SEM images in Figure 29 clearly show that the structure is maintained after carbonisation and can be used for fuel cell testing. It appears that the polymer precursor has a significant impact on the resulting carbon morphology as shown by Figure 30:

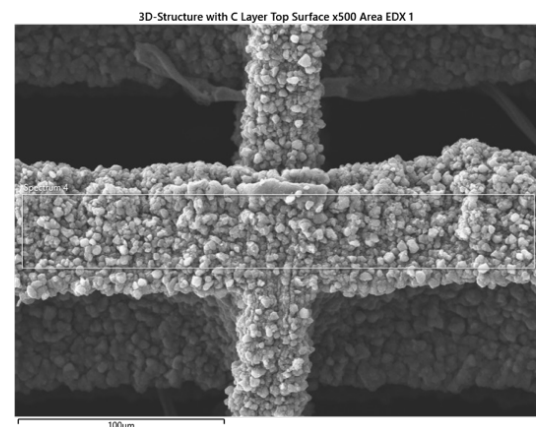


Figure 30 - Close up SEM of carbonised material, showing high surface roughness carbon

During the course of the project, the 3D printer screen was damaged. Therefore, for a period we had to print the electrodes vertically. At the time this was not an issue and it was difficult to see any changes to the microstructure without further analysis.

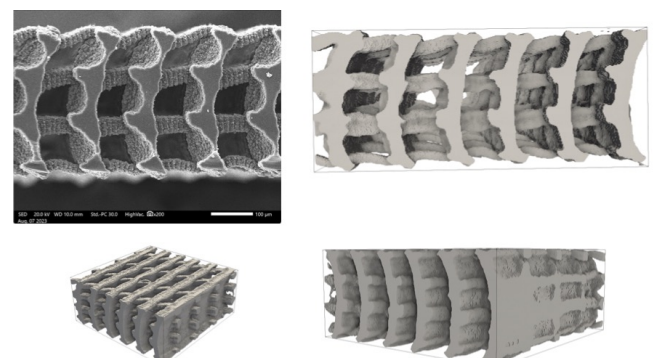


Figure 31 - SEM image of printed material cross-section and X-ray tomography of the same sample at different angles

Figure 31 shows the cross-section of the electrode and X-ray computed tomography results. The structure was

deformed and had walls which cut connectivity of the pore space in one direction. These results have only been presented recently and therefore we did not know that these walls were present without the CT, which could significantly impact the fuel cell performance results.

Catalyst ink

A catalytic ink was prepared by employing 20 wt.% Pt/C, a dispersion of PTFE in water (60 wt.%), Nafion™ 117 containing solution (~5% in a mixture of lower aliphatic alcohols and water), and a solvent of IPA. The designated loading of Pt for both the anode and cathode was proposed to be 0.35 mg/cm², utilizing fourfold the amount of 20 wt.% Pt/C to offset any waste and to realize the required loading. The PTFE dispersion was diluted to a concentration of 5 wt.%, whereas Nafion™ 117 containing solution functioned as an ionomer. PTFE and the Nafion™ 117 containing solution constituted 40 and 30 wt.% of the total weight of 20 wt.% Pt/C, respectively. IPA volume was one-tenth of the total quantity of 20 wt.% Pt/C.

The process commenced with the introduction of the computed weight of 5 wt.% PTFE dispersion and Nafion™ 117 containing solution to the quantified volume of IPA, while concurrently, the calculated quantity of 20 wt.% Pt/C was integrated into a separate bottle with the addition of two droplets of water. Subsequently, the mixture of PTFE and IPA was added to the Pt/C and water bottle. The resultant ink underwent a sonication process for five minutes.

MEA hot pressing

This approach included coating the 3D GDL and anode (Freudenberg H23C9) with PTFE, a Microporous Layer (MPL), and a Catalyst Layer (CL). After that, Nafion 212 was sandwiched between the two electrodes and submitted to hot pressing under 180 psi and 120°C for 2 mins.

Given the size of the pores in the 3D GDL, up to 100 µm, traditional spraying methods (in a vertical position) proved ineffective. However, placing the 3D electrode horizontally allowed for the successful deposition of PTFE, the MPL and CL, as these materials rested on the surface.

PTFE treatment

The 3D GDL's hydrophobicity was augmented through PTFE treatment. A solution of 5 wt.% PTFE was prepared from a PTFE dispersion in water (60 wt.%). 200 µl of this solution was combined with 200 µl of IPA and sprayed onto the 3D GDL's surface. This procedure was reiterated five times, achieving a loading of 15 wt.%. It's noteworthy that while commercial GDLs typically involve 5 wt.% PTFE, the 3D GDL demanded a thrice loading due to its high porosity with a coating on one side only. Thus, post sintering at 300°C for 3 hours, the PTFE would

permeate the pores, ensuring comprehensive hydrophobicity throughout the 3D structure.

MPL coating and Sintering

Post PTFE treatment, a MPL was applied. It consisted of 10 wt.% PTFE and 90 wt.% carbon black (Vulcan XC 72R). A total MPL loading of 5.5 mg/cm² was attained. After the MPL and PTFE coatings, the sample was sintered in a tube furnace under an N₂ atmosphere for 3 hours at 300°C.

CL coating

Following the sintering step, the CL was applied. The catalyst ink used to prepare the CL included a Pt loading of 0.35 mg/cm², 30 wt.% Nafion™ 117 containing solution as an ionomer, and 40 wt.% of 5 wt.% PTFE solution as a binder while using IPA as a solvent.

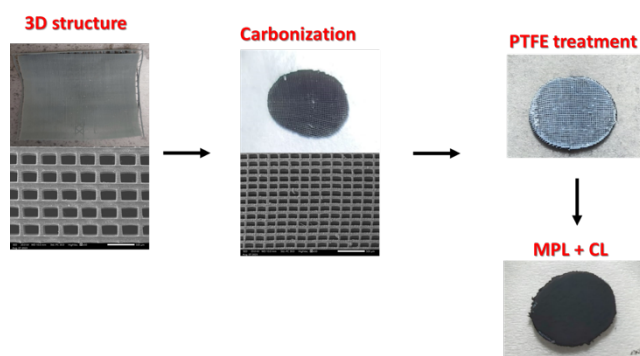


Figure 32 – preparation of the 3D printed electrodes, carbonisation, PTFE treatment and CL coating

Single sided catalyst coated membrane

This approach involves coating Nafion 212 directly with the cathodic CL. Concurrently, the anodic catalyst layer is applied on a commercial GDL (Freudenberg H23C9) coupled with a MPL, specifically, the Freudenberg H23C9, which already undergoes a hydrophobic treatment, ensuring optimal performance in the LT-PEMFC.

Challenges

A pressing challenge faced during the coating process was the shrinkage of the Nafion membrane. This occurs as a reaction to the IPA solvent present in the catalyst ink. When sprayed onto the Nafion, the membrane would contract, leading to an uneven surface along with wrinkles. Such an uneven surface reduces Nafion efficiency.

To counteract the shrinkage issue, a novel approach was employed. Before the coating process

commenced, the Nafion membrane was hot pressed together with the anode electrode. This procedure, conducted at 120°C and applying 180 psi pressure, was maintained for a duration of 2 minutes. The hot-pressing treatment not only prepped the membrane for the subsequent coating but also prevented the formation of any wrinkles, ensuring a smooth, uniform surface. Post hot pressing, the uncoated side of the Nafion membrane was then layered with the cathodic catalyst layer. By adhering to this sequential process, a homogeneous and efficient catalyst layer was achieved on the Nafion membrane as shown by Figure 33.

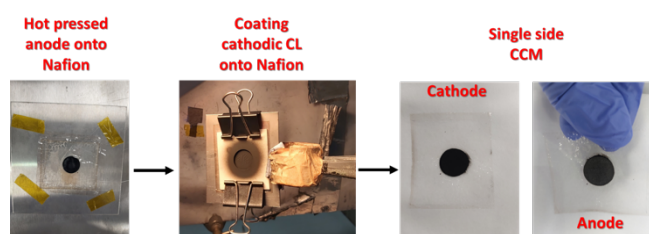


Figure 33 - Single Sided CCM approach

Fuel Cell assembly and testing

The MEA was positioned between two titanium blocks, forming an active electrode area of 1 cm² through a region featuring gold-plated, parallel gas flow channels. To regulate and maintain the required temperature, electric cartridge heaters were integrated into the titanium blocks. The actual temperature was monitored by embedded thermocouples and was systematically managed by a temperature controller. Humidified H₂ and O₂ gases (100% RH) were channeled to each side of the cell, maintaining a flow rate of 250 ml/min while keeping the cell temperature at 60°C. The cell design and the Fuel Cell System are shown in Figure 34 and Figure 35.

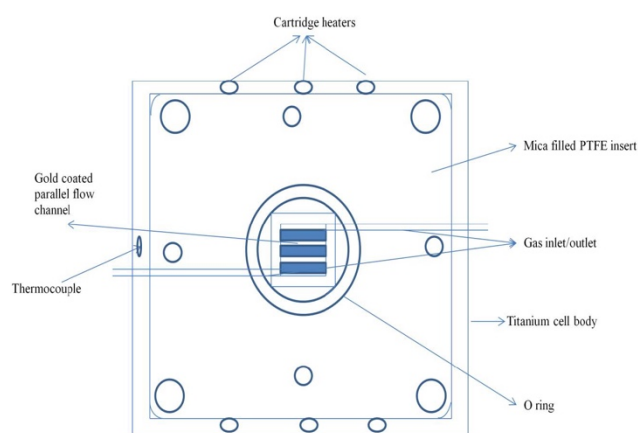


Figure 34 - Illustration of a segment of the titanium cell utilized for through-plane conductivity assessment. The corresponding cell block is analogous in structure.

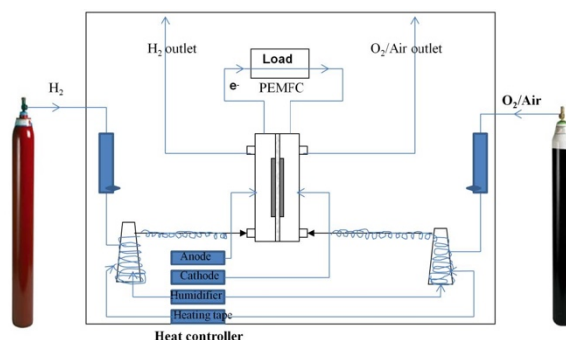


Figure 35 - Schematic Illustration of the Fuel Cell System

Electrochemical tests

Prior to the execution of polarization studies, the cell underwent activation at 0.6 V for a duration of four hours. Electrochemical data were acquired using an Autolab PGSTAT 302N potentiostat, supplied by Eco Chemie, The Netherlands. Polarization curves were collected by applying a cathodic sweep from 1 to 0 V vs. RHE, maintaining a scan rate of 2 mV/s.

Electrochemical impedance spectroscopy (EIS) was collected under fuel cell conditions (H₂-O₂) by applying a constant potential of 0.4 V and sweeping the frequency between 10 kHz and 0.1 Hz with AC amplitude of 10 mV. The electrolyte resistance obtained from Nyquist plot. The through plane ionic conductivity was calculated utilizing the equation:

$$\sigma \text{ (mS/cm)} = \frac{\text{Thickness (cm)}}{\text{Resistance } (\Omega) \times \text{Area (cm}^2\text{)}}$$

To assess H₂ crossover, N₂ gas was supplied to the cathode (serving as the working electrode), while H₂ was supplied to the anode (acting as the counter and reference electrode CE/RE). LSV was employed to document the current related to hydrogen oxidation. The working electrode was subjected to a scan in the range of 0 to 1 V versus CE/RE at a scan rate of 5 mV/s at temperatures of 80 and 110°C. The flux of H₂ crossover (J) (mol.cm⁻².s⁻¹) can be calculated through:

$$J = \frac{I_{lim}}{nF}$$

Where I_{lim} is the limiting current density (A/cm²), n is the number of electrons and F is the Faraday constant (96485 C/mol).

EIS measurements

Electrochemical Impedance Spectroscopy (EIS) assessments of the Membrane Electrode Assembly (MEA) created through hot pressing indicated that Nafion 212 possesses a resistance of 0.24 Ω. This corresponds to a through-plane ionic conductivity of 8.2 mS/cm. As a result, the area-specific resistance stands at 0.24 Ω.cm². This is approximately threefold higher than the value seen with Nafion 212 paired with

commercial GDLs ($0.071 \Omega \cdot \text{cm}^2$) under analogous conditions of 100% RH and 60°C . Such a discrepancy can be attributed to the preliminary treatment of Nafion before testing. This treatment involved the use of hydrogen peroxide to cleanse the Nafion surface from impurities and a subsequent sulfuric acid treatment to substitute Na^+ ions with H^+ ions. Single-sided CCM approach showed almost the same membrane resistance of 0.24Ω as shown on Figure 36.

The calculated Area-Specific Resistance (ASR) offers a deeper understanding of voltage reductions caused by ohmic losses, with further insights available from the polarization data. As illustrated in Figure 36, the peak current density achieved at 0 V vs. RHE is approximately 1000 mA/cm^2 . Utilizing the ASR, the voltage losses stemming from ohmic resistance can be determined using the equation below, resulting in a value of 0.24V . Therefore, from the total 1000 mV applied to produce the 1000 mA/cm^2 at 0 V vs. RHE, only 240 mV is lost due to membrane resistance.

$$\text{Voltage loss (V)} = \text{ASR } (\Omega \cdot \text{cm}^2) \times \text{Current Density (A/cm}^2\text{)}$$

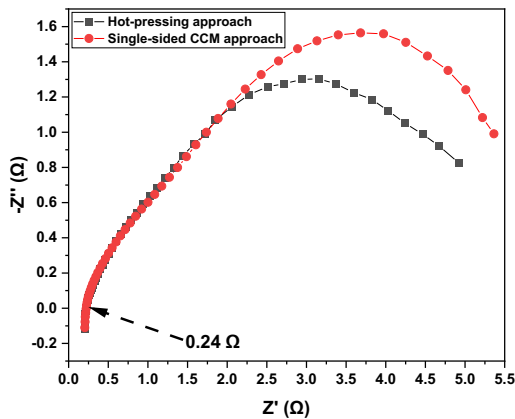


Figure 36 - EIS of MEA under fuel cell conditions of 60°C , 100% RH, and 250 ml flow rates of H_2 and O_2 and 0.4 V .

H₂ crossover testing

For the Membrane Electrode Assembly (MEA) fabricated using the hot-pressing method, the H_2 crossover test indicated a failure in the Nafion, as evidenced by the notably high oxidation current density of 85 mA/cm^2 . This corresponds to a H_2 flux of $4.4\text{E-}07 \text{ mol.cm}^{-2}.\text{s}^{-1}$, which is significantly greater by nearly two orders of magnitude compared to the $2.04\text{E-}08 \text{ mol.cm}^{-2}.\text{s}^{-1}$ seen with Nafion when commercial GDLs were employed for both anode and cathode under comparable test conditions.

Conversely, the single-sided CCM approach exhibited a H_2 oxidation current density of approximately 6.5 mA/cm^2 , marking a reduction by roughly 13 times from the prior test. This leads to a H_2 crossover flux of $3.37\text{E-}8 \text{ mol.cm}^{-2}.\text{s}^{-1}$, closely aligning with the $2.04\text{E-}08 \text{ mol.cm}^{-2}.\text{s}^{-1}$ observed for Nafion with commercial GDLs. Such outcomes underscore the effectiveness of

employing a single-sided CCM to safeguard the MEA from potential damage as shown by Figure 37.

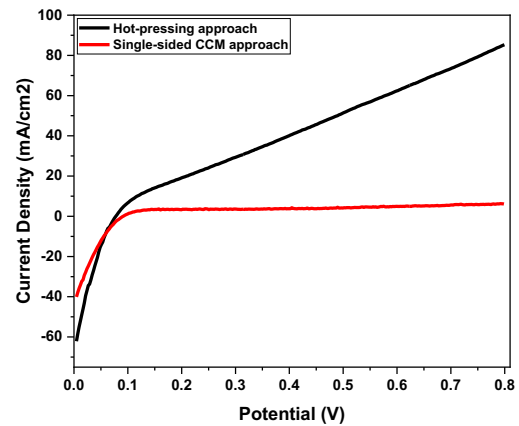


Figure 37 - H_2 crossover test for different electrode integration method

Polarisation curve

During the cathodic sweep from 1 to 0 V, executed at a scan rate of 2 mV/s , the cell employing the hot-pressing method exhibited an OCP of 0.75 V vs. RHE. This value is notably lower than the approximately 1 V vs. RHE observed with Nafion in conjunction with commercial GDL. Additionally, the maximum current density registered was around 1000 mA/cm^2 at 0 V vs. RHE, which is below the $1500\text{--}1800 \text{ mA/cm}^2$ typically seen with Nafion at lower overpotential of 0.6 V vs. RHE, shown in Figure 38.

Conversely, the single-sided CCM method, which demonstrated reduced H_2 crossover, yielded a higher OCP value of 0.95 V vs. RHE. However, its maximum current density remained relatively subdued at 1000 mA/cm^2 at 0 V vs. RHE. Further insights into the cause of this suboptimal performance could be gleaned from SEM analysis (Figure 39).

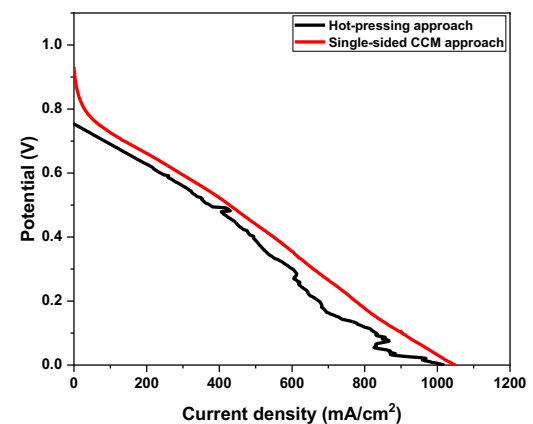


Figure 38 - Polarisation curves for hot pressed and single-sided CCM approach

SEM Analysis of cell

The cross-sectional analysis of the MEA, fabricated through the hot-pressing method, revealed post-test damage to both the Nafion and the 3D electrode. The damage to the 3D electrode during the hot-pressing phase led to its layers sliding and forming sharp, overlapping edges. These edges subsequently punctured the Nafion, creating pinholes. Such perforations likely contributed to the elevated hydrogen crossover, as evidenced by the reduced OCP value of 0.75 V. Additionally, the surface of the 3D electrode bore the imprints of the flow channel ribs, which disrupted the electrode's structure. This resulted in diminished in-plane ionic conductivity and a reduced cathodic active area. Hence, the damage to the MEA was a primary factor in the observed loss in both potential and current density.

In contrast, when the hot-pressing step was avoided via the single-sided method, the MEA's cross-sectional analysis indicated reduced harm to the Nafion. However, the surface still displayed fractures within the 3D electrode, likely inflicted by the flow channel ribs during cell assembly under a 1.5 N.m torque. Consequently, while the OCP did rise to 0.95 V vs. RHE, the current density remained on the lower end, approximately 1000 mA/cm² at 0 V vs. RHE (**Figure 39 and 40**).

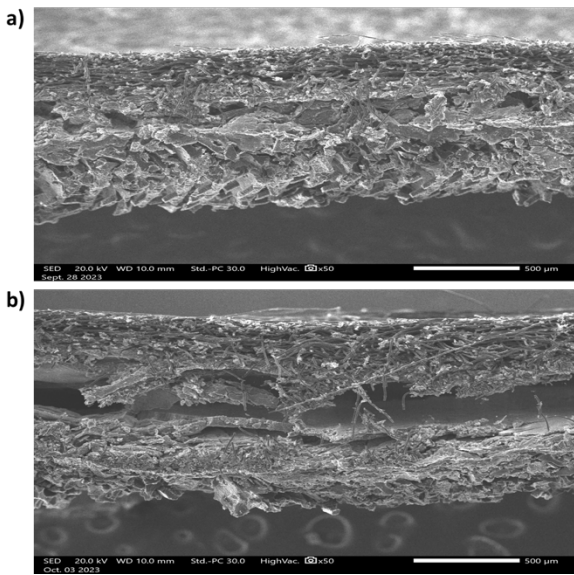


Figure 39 - SEM showing cross section of MEA a) hot pressing approach b) single-sided CCM approach.

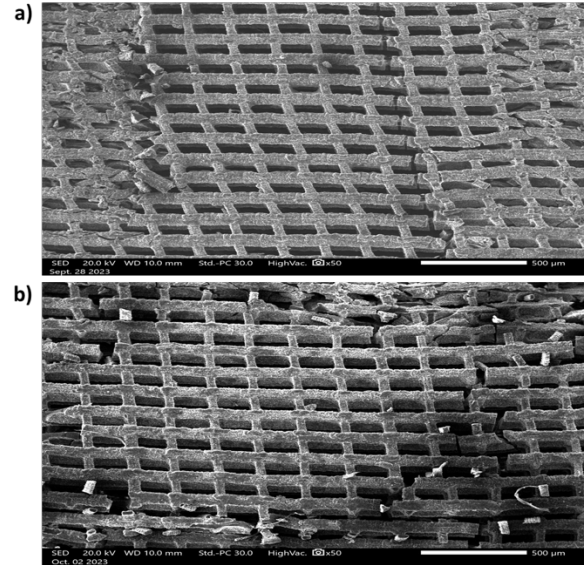


Figure 40 - SEM showing surface morphology of 3D cathodic electrode a) hot pressing approach b) single-sided CCM approach.

Mechanical testing

Compression testing was executed at ambient conditions for 3D GDL after PTFE treatment and coating with MPL and CL (including sintering step), utilizing a TA XT Plus texture analyzer, supplied by Stable Micro Systems, UK. Samples (8 mm diameter) were affixed to a holder, and a probe with a 10 mm diameter was deployed to exert a maximal compressive force of 1.5 g. This minimal force was intended to compress the sample without exceeding the elastic region, where the initial linear section of the stress-strain curve corresponds to Young's modulus. The procedure was reiterated thrice for every sample, and the average values were utilized for the final analysis.

The compression stress was calculated as per:

$$\sigma = \frac{F}{A}$$

Here, σ signifies the compression stress (MPa), F denotes the force exerted by the probe (N), and A represents the cross-sectional area of the probe (m²). Strain was calculated using:

$$\text{Strain \%} = \frac{\Delta T}{T}$$

In this equation, ΔT denotes the alteration in the sample's thickness and T represents the original thickness of the sample.

The findings indicate that the 3D GDL possesses a slope of 0.05, which is 2.5 times steeper than the commercial GDL's 0.02. This suggests that the 3D GDL is more rigid than its commercial counterpart. This is further corroborated by the 3D GDL's lower strain percentage of 3%, in contrast to the commercial GDL, which is more flexible and exhibits a strain percentage of 7%. It underscores the need to enhance the 3D GDL,

aiming for increased flexibility and reduced rigidity
Figure 41.

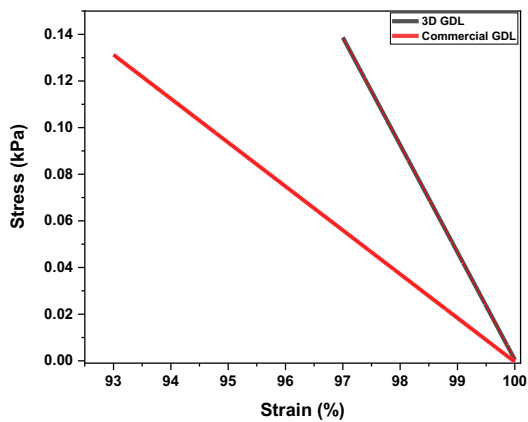


Figure 41 - Stress-strain curve of 3D printed and commercial GDLs

Conclusions and future study

Enhancing the flexibility of 3D printed materials can be a challenge. This might involve carefully adjusting the precursor resin to yield a print that remains flexible after carbonization. Another way might be to make the material harder. The primary goal of using the 3D material as a cathode in LT-PEMFC is to optimize water management, which pivots on preserving the 3D structure. To this end, we experimented with ELEGOO Water Washable Resin, following the same printing specifications as with Phrozen Aqua 8K Resin. Notably, after carbonization, the ELEGOO resin exhibited a greater Young's modulus than the Phrozen Aqua 8K Resin. With a modulus of 0.1, it's effectively twice as hard as the Phrozen Aqua 8K Resin (0.05). This was further verified by strain measurements, with the ELEGOO resin showing a minimal strain of less than 2%, compared to the 3% strain from the Phrozen Aqua 8K Resin:

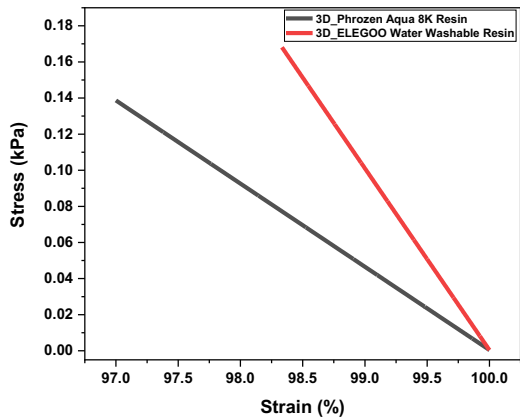


Figure 42 - stress-strain curve of 3D material produced using two different resins

The single-sided CCM method seems promising, as

evidenced by the increased OCP to 0.95 V vs. RHE (Figure 38). This can be attributed to avoiding the hot-pressing step, resulting in minimal damage to the MEA. Yet, the 3D material's fragility made it vulnerable to the pressure during cell assembly at a torque of 1.5 N.m, a necessary step for ensuring gas sealing. In theory, if this challenge is addressed, we might enhance the current density to match or even surpass that of commercial GDLs.

We conducted a preliminary test with the 3D material using the ELEGOO Water Washable Resin to see if it would remain undamaged after assembling the cell at a torque of 1.5 N.m. Positively, the material stayed completely intact Figure 40 displays the MEA post-assembly, clearly highlighting the imprints of the flow channel ribs on both the anode and cathode, indicative of good MEA contact. Moreover, the 3D cathode appears intact.

Moving forward, we're considering using a commercial Hydrogen Air CCM - 3 Layer (from Fuel Cell Store) with a Pt loading of 0.5 mg/cm². This would eliminate the need for the hot-pressing step. Given that we can now maintain the 3D cathode electrode's integrity during testing, we anticipate observing the intended water management improvements with enhanced current and power densities.

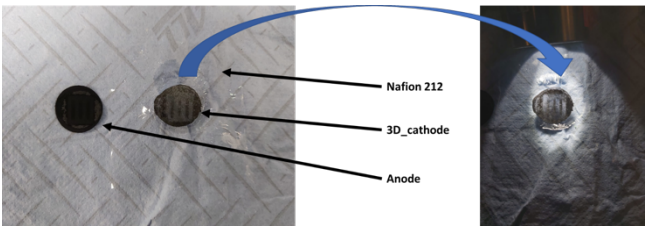


Figure 43 - MEA after cell assembly under a torque of 1.5 N.m showing the 3D-cathode still intact.

Conclusion & Future Work

Conclusions

This study was able to test the feasibility of four different interconnected sub-projects:

1. Prediction of microstructural performance
2. Optimisation of microstructures
3. Neural network training on simulation data
4. 3D printing and integration in fuel cells

It is clear from the results presented in this report that it is possible to meet each of these objectives, although further research is required to fully establish a framework that can seamlessly integrate these areas. This is especially difficult as each area is multi-disciplinary: computational engineering (1), AI optimisation (2), machine learning (3), electrochemistry and manufacturing (4).

In this study, carbonised 3D printed electrodes designed from digital modelling and simulations were able to be manufactured and tested in an operating fuel cell environment. Pore radius of 50 μm and fibre radius of 10 μm were resolvable in this study. Many challenges still remain to enable testing and scale up of the manufacturing and testing.

Future Work

The algorithms developed during this study should be further developed, especially the evolutionary algorithm which shows promise to be coupled to more complex, opensource modelling packages such as OpenFOAM for computational fluid dynamics. It is the goal of the PI to pursue this, using the evolutionary algorithm to predict, design and manufacture metal-based electrodes and materials for PEM, alkaline and membraneless electrolysis for hydrogen production.

Contact & Resources

Project Investigator

Dr. Daniel Niblett – Research Associate, Newcastle University (daniel.niblett@newcastle.ac.uk)

www.danielniblett.com

Niblett, Daniel; Mamlouk, Mohamed; Emmanuel Godinez Brizuela, Omar; An, Senyou (2022). Porous Microstructure Generator. Newcastle University. Software.

<https://doi.org/10.25405/data.ncl.20448471.v7>

connected everything.

industrial systems in the digital age

Dr. Daniel Niblett – daniel.niblett@newcastle.ac.uk

